

INTERPRETATION OF THE UNPRECEDENTEDLY LONG-LIVED HIGH-ENERGY EMISSION OF GRB 130427A

RUO-YU LIU^{1,2,4,*}, XIANG-YU WANG^{1,4} AND XUE-FENG WU^{3,5,6}

¹School of Astronomy and Space Science, Nanjing University, Nanjing, 210093, China

²Max-Planck-Institut für Kernphysik, 69117 Heidelberg, Germany

³Purple Mountain Observatory, Chinese Academy of Sciences, Nanjing 210008, China

⁴Key laboratory of Modern Astronomy and Astrophysics (Nanjing University), Ministry of Education, Nanjing 210093, China

⁵Chinese Center for Antarctic Astronomy, Nanjing 210008, China

⁶Joint Center for Particle, Nuclear Physics and Cosmology, Nanjing University-Purple Mountain Observatory, Nanjing 210008, China

*Fellow of the International Max Planck Research School for Astronomy and Cosmic Physics at the University of Heidelberg (IMPRS-HD)

Draft version February 27, 2018

ABSTRACT

High energy photons (> 100 MeV) are detected by the *Fermi*/LAT from GRB 130427A up to almost one day after the burst, with an extra hard spectral component being discovered in the high-energy afterglow. We show that this hard spectral component arises from afterglow synchrotron-self Compton emission. This scenario can explain the origin of > 10 GeV photons detected up to ~ 30000 s after the burst, which would be difficult to be explained by synchrotron radiation due to the limited maximum synchrotron photon energy. The lower energy multi-wavelength afterglow data can be fitted simultaneously by the afterglow synchrotron emission. The implication of detecting the SSC emission for the circumburst environment is discussed.

Subject headings: gamma ray: bursts — radiation mechanism: non-thermal

1. INTRODUCTION

The extended high-energy emission detected by *Fermi*/LAT is widely believed to arise from the electrons accelerated in the external-forward shock via the synchrotron radiation (e.g. Kumar & Barniol Duran 2009, 2010). However, the maximum photon energy in this scenario is limited to be $\epsilon_{\gamma, \max} = 50\Gamma$ MeV, where 50 MeV is the maximum synchrotron photon in the rest frame of the shock and Γ is the bulk Lorentz factor of the shock, which is usually $\lesssim 300$ at ~ 100 s after the trigger (e.g. Piran & Nakar 2010; Barniol Duran & Kumar 2011). So the detection of > 10 GeV photons after 100 s poses a challenge for the synchrotron emission scenario (Piran & Nakar 2010; Sagi & Nakar 2012). Considering the above difficulty, Wang et al. (2013) recently proposed that the afterglow synchrotron self-Compton (SSC) emission or external inverse-Compton of central X-ray emission (Wang et al. 2006) is likely responsible for the late-time > 10 GeV photons seen in some LAT GRBs.

GRB 130427A triggered the *Fermi*/GBM with a fluence of 2×10^3 erg cm⁻² in 10-1000 keV within a duration of $T_{90} = 138$ s (von Kienlin 2013). It was later localized at $z \simeq 0.34$ (Flores et al. 2013; Levan et al. 2013; Xu et al. 2013a), implying an isotropic energy of 7.8×10^{53} erg (Kann & Schulze 2013). Unprecedentedly, > 100 MeV emissions are detected well beyond the prompt emission phase up to about one day after the burst, including fifteen > 10 GeV photons detected up to ~ 30000 s and one 95.3 GeV photon arrived at 243s after the trigger (Zhu et al. 2013; Tam et al. 2013). It was suggested that these late-time high-energy photons may arise from inverse-Compton processes (Fan et al. 2013; Wang et al. 2013). Further evidence comes from the presence of a hard spectral component (the photon index $\Gamma_{\text{ph}} = -1.4 \pm 0.1$) above 2.5 ± 1.1 GeV (Tam et al. 2013) in the late afterglow, which has signatures well consistent with the prediction of the afterglow synchrotron self-Compton emission (Zhang & Mészáros 2001; Sari & Esin 2001; Zou et al. 2009). In this Letter, we will verify this possibility by mod-

eling the multi-band (from radio to GeV bands) data of this burst. Hereafter, we denote by Q_x the value of the quantity Q in units of 10^x .

2. A BRIEF OVERVIEW OF THE MODEL

In the standard synchrotron afterglow spectrum, there are three break frequencies, i.e. ν_a , ν_m and ν_c , which are caused by synchrotron self-absorption (SSA), electron injection and electron cooling respectively. According to (e.g. Sari et al. 1998; Wijers & Galama 1999), these three characteristic frequencies are given by

$$\nu_m = 1.1 \times 10^{18} f^2(p) \epsilon_{e,-1}^2 E_{54}^{1/2} \epsilon_{B,-5}^{1/2} (1+z)^{1/2} T^{-3/2} \text{Hz}, \quad (1)$$

$$\nu_c = 1.1 \times 10^{17} E_{54}^{-1/2} n_0^{-1} \epsilon_{B,-5}^{-3/2} \left(\frac{1+Y}{100} \right)^{-2} (1+z)^{-1/2} T^{-1/2} \text{Hz}, \quad (2)$$

and

$$\nu_a = 2.7 \times 10^{10} f^{-1}(p) E_{54}^{1/5} \epsilon_{e,-1}^{-1/5} \epsilon_{B,-5}^{1/5} n_0^{3/5} (1+z)^{-1}, \quad (3)$$

in the case that $\nu_a < \nu_m < \nu_c$, which is usually true under typical parameter values. In the above three equations, T is the time in the observer's frame since the trigger time, z is the redshift of the burst, $f(p) = 6(p-2)/(p-1)$ with p being the electron index, E is the isotropic kinetic energy of the GRB outflow and n is the number density of the circumburst medium. For an interstellar medium (ISM) circumburst environment, n is a constant while for a stellar wind circumburst environment, it is inversely proportional to the square of the shock radius. ϵ_e and ϵ_B are the equipartition factors for the energy in electrons and magnetic field in the shock respectively. In the expression of ν_c , Y is the Compton parameter evaluating the effect of SSC cooling on the synchrotron spectrum. In the Thomson scattering limit, $Y = Y_0 \simeq \left(\frac{\epsilon_e}{\epsilon_B} \right)^{\frac{1}{4-p}} \left(\frac{\nu_m}{\nu_{c,\text{syn}}} \right)^{\frac{p-2}{2(4-p)}}$ (Sari & Esin 2001) if $Y \gg 1$, where $\nu_{c,\text{syn}}$ is obtained by considering only the synchrotron cooling.

The time-integrated spectrum of high-energy emission from GRB 130427A can be modeled by a broken power-law with a soft component ($\Gamma_{\text{ph}} = 2.3 \pm 0.1$) below the break energy $E_b = 2.5 \pm 1.1$ GeV and a hard component ($\Gamma_{\text{ph}} = 1.4 \pm 0.1$) above E_b (Tam et al. 2013). It is natural to assume that synchrotron emission is dominant below E_b while the SSC emission is dominant above E_b . As Tam et al. (2013), we assume $p = 2.2$ in the following analysis. Thus, the synchrotron flux at $h\nu_c < 100\text{MeV} \leq h\nu_{\text{LAT}} < E_b$ is given by

$$F_\nu(100\text{MeV}) = 7.0 E_{54}^{1.05} \epsilon_{e,-1}^{1.2} \epsilon_{B,-5}^{0.05} (1+z)^{1.05} \times D_{L,28}^{-2} T^{-1.15} \left(\frac{h\nu}{100\text{MeV}} \right)^{-1.1} \mu\text{Jy} \quad (4)$$

where D_L is the luminosity distance. Here we neglect the inverse-Compton cooling for the electrons that radiate high-energy gamma-ray emission due to the deep Klein-Nishina (KN) scattering effect (Wang et al. 2010; Liu & Wang 2011). The emission above E_b can be interpreted as the SSC emission in the regime of $h\nu_m^{\text{SSC}} < h\nu_{\text{LAT}} < h\nu_c^{\text{SSC}}$, where ν_m^{SSC} and ν_c^{SSC} are the corresponding break frequencies in the SSC spectrum. The SSC flux is given by (Sari & Esin 2001)

$$F_\nu(10\text{GeV}) = 5.6 \times 10^{-3} E_{54}^{1.7} n_0^{1.1} \epsilon_{e,-1}^{2.4} \epsilon_{B,-5}^{0.8} (1+z)^{1.5} \times D_{L,28}^{-2} T^{-1.1} \left(\frac{h\nu}{10\text{GeV}} \right)^{-0.6} \mu\text{Jy} \quad (5)$$

Lower energy emission is produced by the forward shock synchrotron radiation. X-ray observation frequency is usually also in the fast cooling regime, i.e. $\nu_m < \nu_c < \nu_X$. But the KN suppression effect is not as important as in the case of $> 100\text{MeV}$ emission, so we need to consider the effect of SSC cooling on the synchrotron spectrum carefully. Thus, we have

$$F_\nu(10\text{keV}) = 17 E_{54}^{1.05} \epsilon_{e,-1}^{1.2} \epsilon_{B,-5}^{0.05} \left[\frac{1+Y(10\text{keV})}{10} \right]^{-1} \times (1+z)^{1.05} D_{L,28}^{-2} T^{-1.15} \left(\frac{h\nu}{10\text{keV}} \right)^{-1.1} \text{mJy} \quad (6)$$

Here $Y(10\text{keV}) = f_{\text{KN}} Y_0$ with $Y_0 = U_{\text{syn}}/U_B = 110 E_{54}^{0.056} n_0^{0.056} \epsilon_{e,-1}^{0.67} \epsilon_{B,-5}^{-0.44} (1+z)^{0.056} T^{-0.056}$ being the Compton parameter in the Thomson scattering limit as mentioned above, where U_{syn} and U_B are the energy density of synchrotron radiation field and magnetic field respectively. The factor f_{KN} considers the KN effect on the electrons that emit 10keV photons by synchrotron radiation. In the Thomson scattering regime $f_{\text{KN}} = 1$, while in the deep KN scattering regime $f_{\text{KN}} \rightarrow 0$.

The KN effect will intervene in the inverse Compton cooling if the energy of the incident photon exceeds the rest energy of the scattering electron in its rest frame, i.e., $\gamma_e h\nu_{\text{KN}}(1+z)/\Gamma \geq m_e c^2$, where γ_e is the Lorentz factor of the electron in the comoving frame of the emitting region and ν_{KN} is the critical frequency of the incidence photon measured in the observer's frame. If the energy of a photon is larger than $h\nu_{\text{KN}}$, the scatter will enter the KN regime with a suppressed cross section. The Lorentz factor of the electron emitting X-ray

photons can be given by $\gamma_{10\text{keV}} = \left(\frac{2\pi m_e c \nu_X (1+z)}{\Gamma e B} \right)^{1/2}$ and thus

$$\nu_{\text{KN},10\text{keV}} = 2.8 \times 10^{18} E_{54}^{1/4} \epsilon_{B,-5}^{1/4} (1+z)^{-3/4} \left(\frac{h\nu_X}{10\text{keV}} \right)^{1/2} T^{-3/4} \quad (7)$$

As $\nu_{\text{KN}} \propto T^{-3/4}$, the KN suppression effect becomes more and more important at later time. As a rough estimate, f_{KN} can be given by

$$f_{\text{KN}} = \frac{U_{\text{syn}}(\nu < \nu_{\text{KN}})}{U_{\text{syn}}} \simeq \begin{cases} 0.06 \left(\frac{\nu_m}{\nu_c} \right)^{0.4} \left(\frac{\nu_{\text{KN}}}{\nu_m} \right)^{4/3} & \nu_{\text{KN}} < \nu_m, \\ 0.2 \left(\frac{\nu_{\text{KN}}}{\nu_c} \right)^{0.4} & \nu_m < \nu_{\text{KN}} < \nu_c, \\ 1 - 0.8 \left(\frac{\nu_{\text{KN}}}{\nu_c} \right)^{-0.1} & \nu_c < \nu_{\text{KN}} \end{cases} \quad (8)$$

In a broad parameter space, we find $\nu_m < \nu_{\text{KN}} < \nu_c$, leading to $f_{\text{KN}} \simeq 0.1 E_{54}^{0.3} n_0^{0.4} \epsilon_{B,-5}^{0.7} (1+z)^{0.1} \left[\frac{1+Y(10\text{keV})}{10} \right]^{0.8} \left(\frac{h\nu}{10\text{keV}} \right)^{0.2} T^{-0.1}$.

Optical emission is typically in the frequency regime $\nu_m < \nu_{\text{Op}} < \nu_c$, so the flux is given by

$$F_\nu(\text{R band}) = 1.3 E_{54}^{1.3} n_0^{0.5} \epsilon_{e,-1}^{1.2} \epsilon_{B,-5}^{0.8} (1+z)^{1.3} \times D_{L,28}^{-2} T^{-0.9} \left(\frac{\nu}{4.56 \times 10^{14}\text{Hz}} \right)^{-0.6} \text{Jy}. \quad (9)$$

The radio observation frequency could lie in the regime $\nu_a < \nu_{\text{Ra}} < \nu_m$ or $\nu_{\text{Ra}} < \nu_a < \nu_m$. In the former case,

$$F_\nu(5\text{GHz}) = 20 E_{54}^{5/6} n_0^{1/2} \epsilon_{e,-1}^{-2/3} \epsilon_{B,-5}^{1/3} (1+z)^{5/6} \times D_{L,28}^{-2} T^{1/2} \left(\frac{\nu}{5\text{GHz}} \right)^{1/3} \mu\text{Jy}, \quad (10)$$

while in the latter case,

$$F_\nu(5\text{GHz}) = 1.3 E_{54}^{1/2} n_0^{-1/2} \epsilon_{e,-1} (1+z)^{5/2} \times D_{L,28}^{-2} T^{1/2} \left(\frac{\nu}{5\text{GHz}} \right)^2 \mu\text{Jy}. \quad (11)$$

We note that in previous works, modeling of the multi-band light curves of LAT-detected GRBs usually result in a low circumburst density $< 10^{-2} \text{cm}^{-3}$ (e.g. Cenko et al. 2011; Liu & Wang 2011; He et al. 2011). In a low-density environment, SSC flux would be severely suppressed. We here point out that the low-density result is mainly due to neglect of the KN effect in modeling the X-ray afterglows. We now briefly show that considering the KN effect in X-ray afterglow can change the inferred density dramatically.

Usually $> 10\text{GeV}$ data are not available, and only $> 100\text{MeV}$, X-ray, optical and radio data are used in the multi-band light curve fit. So from Eqs. (4), (6), (9), and (10) or (11), we get four independent constraints on four undetermined parameters, namely E , n , ϵ_e and ϵ_B (note that $p = 2.2$ is fixed). So we can fully determine these parameters by solving these equations. In the case that KN effect is not considered in X-ray emission, i.e., $f_{\text{KN}} = 1$, we get

$$\begin{cases} E \simeq C_{\text{LAT}}^{0.74} C_X^{0.45} C_{\text{Op}}^{0.59} C_{\text{Ra}}^{0.64} \\ n \simeq C_{\text{LAT}}^{0.28} C_X^{-2.26} C_{\text{Op}}^{1.09} C_{\text{Ra}}^{0.66} \\ \epsilon_e \simeq C_{\text{LAT}}^{0.26} C_X^{-0.45} C_{\text{Op}}^{0.48} C_{\text{Ra}}^{-0.53} \\ \epsilon_B \simeq C_{\text{LAT}}^{-1.77} C_X^{1.35} C_{\text{Op}}^{0.80} C_{\text{Ra}}^{-0.65} \end{cases} \quad (12)$$

Here we adopt the case that $\nu_a < \nu < \nu_m$ for radio flux as an example. C_{LAT} , C_X , C_{Op} and C_{Ra} are constants related to data

used to normalize the flux in LAT, X-ray, optical, radio band respectively.

When considering the KN effect in X-ray, as long as $Y = f_{\text{KN}} Y_0 \gtrsim 1$, we can approximately replace the C_X by $C_X f_{\text{KN}}$ in the above equation set and we then get

$$\begin{cases} E = f_{\text{KN}}^{0.45} \hat{E} \\ n = f_{\text{KN}}^{-2.26} \hat{n} \\ \epsilon_e = f_{\text{KN}}^{-0.45} \hat{\epsilon}_e \\ \epsilon_B = f_{\text{KN}}^{1.35} \hat{\epsilon}_B. \end{cases} \quad (13)$$

Here we denote the parameters without considering the KN effect on X-ray emission by hatted characters. If $f_{\text{KN}} Y_0 \ll 1$, f_{KN} should be replaced by $(1 + Y_0)^{-1}$ in the above equation set. Since $f_{\text{KN}} < 1$, considering the KN effect in X-ray emission will increase the inferred ISM density significantly. Substituting Eq. (13) into Eq. (5), we find $F_{\nu, \text{IC}} \simeq f_{\text{KN}}^{-1.7} \hat{F}_{\nu, \text{IC}}$, so the SSC flux can be significantly increased as well.

Here we would like to point out that Eq. (8) underestimates the value of f_{KN} because the scattering cross section in the KN regime is approximated as being zero. In our numerical code, we calculate f_{KN} as

$$f_{\text{KN}} = \frac{\int_0^{\nu_{\text{KN}}} F_{\nu} d\nu + \int_{\nu_{\text{KN}}}^{\infty} [2 \ln(2\gamma_e h\nu / \Gamma m_e c^2) + 1] (\frac{\nu}{\nu_{\text{KN}}})^{-1} F_{\nu} d\nu}{\int_0^{\infty} F_{\nu} d\nu}, \quad (14)$$

where the expression before F_{ν} in the second integration on the numerator accounts for the correction to the scattering cross section above ν_{KN} .

3. FITTING OF THE MULTI-BAND LIGHT CURVE DATA

There are abundant observational data of the multi-band light curves of GRB 130427A. The extended high-energy emission in the energy range 0.1-2 GeV and 2-100 GeV shows a power-law decay with slopes of $\alpha_1 = 1.1 \pm 0.1$ and $\alpha_2 = 1.0 \pm 0.1$ respectively (Tam et al. 2013). Therefore we adopt the ISM density profile for the circumburst environment, because in the wind environment, the late-time SSC flux would decrease much faster than the observed one¹.

According to the Fermi/LAT spectral data shown in (Tam et al. 2013), the 0.1-2 GeV flux is dominated by the synchrotron component. Requiring the synchrotron flux be $10^{-4} \text{ ph cm}^{-2} \text{ s}^{-1}$ at 300s, we obtain

$$E_{54}^{1.05} \epsilon_{e,-1}^{1.2} \epsilon_{B,-5}^{0.05} = 1.5. \quad (15)$$

And, by requiring the SSC flux be $3 \times 10^{-7} \text{ ph cm}^{-2} \text{ s}^{-1}$ at 5000s in 2-100 GeV, we obtain

$$E_{54}^{1.7} \epsilon_{e,-1}^{2.4} \epsilon_{B,-5}^{0.8} n_0^{1.1} = 20. \quad (16)$$

The XRT data show that the X-ray flux decay with a slope of -1.2 since 421s after the trigger, then breaks at 53.4ks to a steeper slope of -1.8 (Evans et al. 2013), and after ~ 1 day the light curve becomes shallower again with a slope of -1.3. The first slope is consistent with the decay of the synchrotron flux when the observation frequency is above the cooling frequency, i.e. $\nu_X > \nu_c$. To explain the second slope, we introduce a jet break around 53.4ks. The late-time shallower decay could be due to the KN suppression effect which becomes more and more important at later times. Since the KN

¹ In the ISM medium, $\nu_{m, \text{IC}} \propto T^{-9/4}$, $F_{\nu_{m, \text{IC}}} \propto T^{1/4}$ and $F_{\nu} = F_{\nu_{m, \text{IC}}} (\nu / \nu_{m, \text{IC}})^{-(p-1)/2} \propto T^{(11-9p)/8}$. While in the wind medium, $\nu_{m, \text{IC}} \propto t^{-2}$ and $F_{\nu_{m, \text{IC}}} \propto t^{-1}$, so $F_{\nu} = F_{\nu_{m, \text{IC}}} (\nu / \nu_{m, \text{IC}})^{-(p-1)/2} \propto t^{-p}$

effect is not easy to express accurately in an analytical way, we include it in the numerical modeling.

The optical flux decreases slowly at early time with a slope of -0.8 (Laskar et al. 2013), which is consistent with the decay slope of synchrotron emission in the frequency regime $\nu_m < \nu_{\text{opt}} < \nu_c$. The light curve becomes obviously steeper after ~ 0.3 day with a slope of -1.35 (Laskar et al. 2013) and then a flattening shows up at ~ 10 days after the trigger (Trotter et al. 2013). The steepening in the light curve can be ascribed to the jet break as well. Although the jet break usually results in a steeper slope than -1.35, we note that there is an emerging supernova component (Xu et al. 2013b), so this shallow slope could be caused by the superposition of the fast decaying synchrotron afterglow component and the supernova component. Since the R-band flux is about 1 mJy at ~ 30 ks, we have

$$E_{54}^{1.3} \epsilon_{e,-1}^{1.2} \epsilon_{B,-5}^{0.8} n_0^{0.5} = 1.8. \quad (17)$$

The radio data starts from ~ 0.67 day after the trigger (Laskar et al. 2013), which is around the assumed jet break time. The observed 5 GHz flux at 0.67 day and 2 days after the trigger are comparable, and decreases by a factor of a few at 4.7 days. This decay can be ascribed to the jet break. Higher frequency observations such as 20 GHz, 36 GHz start later and show a decaying light curve from the beginning. By requiring that the synchrotron flux at 5 GHz flux be 2 mJy at 0.67 day, we get

$$E_{54}^{0.5} \epsilon_{e,-1} n_0^{0.5} = 0.9. \quad (18)$$

The early radio emission can be also attributed to the reverse shock emission, as suggested by Laskar et al. (2013)². Then we will require that the flux produced by the forward shock is below the observed flux. This is possible in the framework of the decaying micro-turbulence magnetic field scenario (Lemoine et al. 2013; Wang et al. 2013), since the radio-emitting electrons radiate in a weaker magnetic field region.

As we can see, the early and late time LAT observations, the optical and the radio observations already provide four independent constraints on four parameters (i.e., E , n , ϵ_e and ϵ_B). Since the X-ray observation can in principle put another constraint independently, the system of equations is overdetermined. Finding a solution for the overdetermined system of equations supports the validity of our model.

By solving the above four equations, we get $E_{54} \simeq 0.3$, $n_0 \simeq 6$, $\epsilon_{e,-1} \simeq 5$, $\epsilon_{B,-5} \simeq 0.5$. Although the analytic solution and numerical solution may not conform each other perfectly, we can use these values as a guide, and fine-tune them to get a good global solution in our numerical code. We show the fitting of multi-band light curves in Fig. 1. The final values of the parameters are not much different from the above values, as shown in the caption of the figure. We also present the light curve of > 100 GeV SSC emission with a purple dashed line. It peaks around 100s with a flux of $10^{-6} \text{ ph cm}^{-2} \text{ s}^{-1}$. Given the LAT effective area of $\sim 10^4 \text{ cm}^2$, one expect that LAT may detect one $\gtrsim 100$ GeV photon in ~ 100 s around the peak time, which is consistent with the detection of the 95.3 GeV photon at 243s after the trigger time. Our model can not explain the high energy emission during the prompt emission phase

² Introducing a reverse shock component helps to explain the observed soft radio spectrum ($F_{\nu} \propto \nu^{\beta}$ with $\beta < 0$) at 2 days and 4.7 days after the trigger time. On the other hand, we also note that radio observations during early time (e.g., < 10 days after the trigger time) may suffer from the interstellar scintillation (Goodman 1997), so the observed flux and spectral index could be affected to some extent.

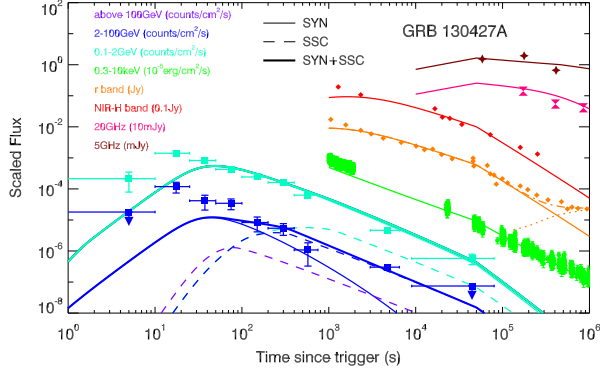


Figure 1. Fit of the multi-band light curves of GRB 130427A. For the high-energy emission, the thin solid lines represent the synchrotron flux, the dashed lines represent the SSC flux and the thick solid lines represents the total flux. The orange dotted line represents the supernova component, which has the same shape as SN1998bw but with a flux normalized to the detected flux. And the orange dashed line is the sum of the GRB afterglow component and the supernova component. The LAT data is taken from (Tam et al. 2013). The X-ray data is taken from the website http://www.swift.ac.uk/xrt_curves. The optical, near-infrared data and radio data are taken from (Laskar et al. 2013). In this fit, we used the following parameter values: $E_k = 2 \times 10^{53}$ erg, $\epsilon_e = 0.6$, $\epsilon_B = 1.3 \times 10^{-5}$, $n = 1 \text{ cm}^{-3}$, $p = 2.2$, $\Gamma_0 = 200$. The jet break time is set at 0.65 day after the trigger time. The opening angle is $\theta_j = 7^\circ$, corresponding to $E_{k,\text{jet}} = 1.5 \times 10^{51}$ erg.

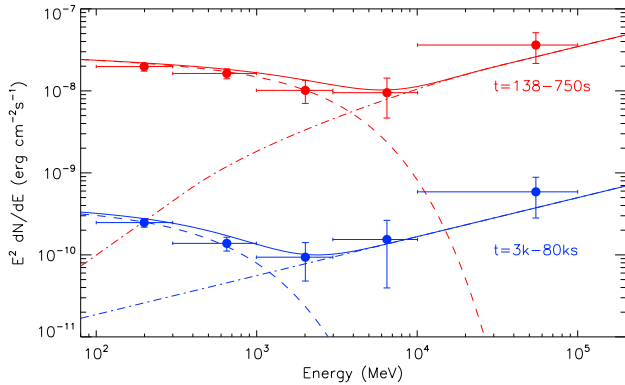


Figure 2. Fit of the spectrum of LAT emission at two different times. The dashed lines and the dash-dotted lines represent the synchrotron component and the SSC component respectively, and the solid lines represent the sum of them.

($\lesssim 100$ s), which is attributed to the internal dissipation origin (He et al. 2011; Liu & Wang 2011; Maxham et al. 2011). In the numerical modeling, we find that $f_{\text{KN}}(10 \text{ keV})$ gradually decreases from $\gtrsim 0.1$ at 1000s to ~ 0.01 at 10^6 s. Fig. 2 presents the fit of the time-integrated spectrum of LAT emission for the period of 138–750 s and 3000–80000 s.

4. DISCUSSIONS

The extended, hard emission above a few GeV, seen in GRB 130427A, represents strong evidence of a SSC component in the forward shock emission. The appearance of the SSC component implies that the circumburst density should not be too low, in contrast to the result in the previous study that the circumburst density of LAT-detected bursts is on average lower than usual (Cenko et al. 2011). The inferred density in this

work is of the same order of the typical ISM density in the galaxy disk where massive stars reside.

Recently, Laskar et al. (2013) modeled the low-energy afterglows of this GRB with a forward-reverse shock synchrotron emission model. However, we find that their model predicts a synchrotron flux about one order of magnitude lower than the observed flux in the LAT energy range. To interpret the multi-band afterglow data including the LAT data, we proposed a forward shock synchrotron plus SSC emission scenario. We also find that an ISM environment is favored by the slow decay of 2–100 GeV flux, which is explained as the SSC origin.

We would like to thank He Gao, Zhuo Li and the anonymous referee for valuable suggestions. This work is supported by the 973 program under grant 2009CB824800, the NSFC under grants 11273016, 10973008, and 11033002, the Excellent Youth Foundation of Jiangsu Province (BK2012011), and the Fok Ying Tung Education Foundation. XFW is partially supported by the National Basic Research Program ("973" Program) of China (Grant 2013CB834900), the One-Hundred-Talents Program and the Youth Innovation Promotion Association of the Chinese Academy of Sciences, and the Natural Science Foundation of Jiangsu Province.

REFERENCES

- Barniol Duran, R., & Kumar, P. 2011, MNRAS, 412, 522
 Cenko, S. B., Frail, D. A., Harrison, F. A., et al. 2011, ApJ, 732, 29
 Evans, P. A., Page, K. L., Maselli, A., Mangano, V., Capalbi, M., Burrows, D. N. 2013, GCN Circ. 14502
 Fan, Y.-Z., Tam, P. H. T., Zhang, F.-W., et al. 2013, arXiv:1305.1261
 Flores, H., Covino, S., Xu, D., et al. 2013, GRB Coordinates Network, 14491, 1
 Goodman, J. 1997, New Astronomy, 2, 449
 He, H. N., Wu, X. F., Toma, K., Wang, X. Y., & Mészáros, P. 2011, ApJ, 733, 22
 Kann, D. A. & Schulze, S. 2013, GCN Circ. 14580, 1
 von Kienlin, A. 2013, GRB Coordinates Network, 14473, 1
 Kumar, P., & Barniol Duran, R. 2009, MNRAS, 400, L75
 Kumar, P., & Barniol Duran, R. 2010, MNRAS, 409, 226
 Laskar, T., Berger, E., Zauderer, B. A., et al. 2013, arXiv:1305.2453
 Lemoine, M., Li, Z., & Wang, X.-Y. 2013, arXiv:1305.3689
 Leván, A. J., Cenko, S. B., Perley, D. A., & Tanvir, N. R. 2013, GCN, 14455, 1
 Liu, R. Y., & Wang, X. Y., 2011, ApJ, 730, 1
 Maxham, A., Zhang, B.-B., Zhang, B., 2011, MNRAS, 415, 77
 Piran, T., & Nakar, E. 2010, ApJ, 718, L63
 Sagi, E., & Nakar, E. 2012, ApJ, 749, 80
 Sari, R., & Piran, T. 1995, ApJ, 455, L143
 Sari, R., Piran, T., & Narayan, R. 1998, ApJ, 497, L17
 Sari, R. & Esin, A. A. 2001, ApJ, 548, 787
 Tam, P.-H. T., Tang, Q.-W., Hou, S.-J., Liu, R.-Y., & Wang, X.-Y. 2013, ApJ, 771, L13
 Trotter, A., Reichart, D., Haislip, J., et al. 2013, GRB Coordinates Network, 14510, 1
 Wang, X.-Y., Li, Z., Mészáros, P. 2006, ApJ, 641, L89
 Wang, X.-Y., He, H.-N., Li, Z., Wu, X.-F., & Dai, Z.-G. 2010, ApJ, 712, 1232
 Wang, X.-Y., Liu, R.-Y., & Lemoine, M. 2013, ApJ, 771, L33
 Wijers, R. A. M. J., & Galama, T. J. 1999, ApJ, 523, 177
 Xu, D., et al. 2013, GCN Circ. 14478, 1
 Xu, D., de Ugarte Postigo, A., Leloudas, G., et al. 2013, arXiv:1305.6832
 Zhang, B., & Mészáros, P. 2001, ApJ, 559, 110
 Zhu, S., Racusin, J., Kocevski, D., McEnery, J., Longo, F., Chiang, J., & Vianello, G. 2013b, GCN Circ. 14508, 1
 Zou, Y.-C., Fan, Y.-Z., & Piran, T. 2009, MNRAS, 396, 1163